This is a copy of the published version, or version of record, available on the publisher's website. This version does not track changes, errata, or withdrawals on the publisher's site.

Superconducting and normal-state properties of the high-entropy alloy Nb-Re-Hf-Zr-Ti investigated by muon spin relaxation and rotation

K. Motla, P. K. Meena, D. Arushi, D. Singh P. K. Biswas, A. D. Hillier,
and R. P. Singh

Published version information

Citation: K Motla et al. Superconducting and normal-state properties of the high-entropy alloy Nb-Re-Hf-Zr-Ti investigated by muon spin relaxation and rotation. Phys Rev B 105, no. 14 (2022): 144501

DOI: 10.1103/PhysRevB.105.144501

This version is made available in accordance with publisher policies. Please cite only the published version using the reference above. This is the citation assigned by the publisher at the time of issuing the APV. Please check the publisher's website for any updates.

This item was retrieved from **ePubs**, the Open Access archive of the Science and Technology Facilities Council, UK. Please contact epublications@stfc.ac.uk or go to http://epubs.stfc.ac.uk/ for further information and policies.

Superconducting and normal-state properties of the high-entropy alloy Nb-Re-Hf-Zr-Ti investigated by muon spin relaxation and rotation

K. Motla,[1] P. K. Meena,[1] Arushi,[1] D. Singh,[2] P. K. Biswas,[2] A. D. Hillier,[2] and R. P. Singh[1,*]

[1]*Department of Physics, Indian Institute of Science Education and Research Bhopal, Bhopal 462066, India*

[2]*ISIS Facility, STFC Rutherford Appleton Laboratory, Harwell Science and Innovation Campus, Oxfordshire OX11 0QX, United Kingdom*

(Received 4 December 2021; accepted 16 March 2022; published 4 April 2022)

Superconducting high entropy alloys (HEAs) are emerging as an exotic class of superconducting materials, providing a unique opportunity to understand the complex interplay of disorder and superconductivity. We report the synthesis and detail bulk and microscopic characterization of a $Nb_{60}Re_{10}Zr_{10}Hf_{10}Ti_{10}$ HEA alloy using transport, magnetization, specific heat, and muon spin rotation/relaxation (μSR) measurements. Bulk superconductivity with transition temperature $T_C = 5.7$ K is confirmed by magnetization, resistivity, and heat capacity measurements. Zero-field μSR measurements confirm that the superconducting state preserves time-reversal symmetry, and transverse-field measurements show that the superfluid density is well described by an isotropic *s*-wave model.

DOI: 10.1103/PhysRevB.105.144501

I. INTRODUCTION

High entropy alloys (HEAs) are a class of multicomponent materials with outstanding mechanical, thermal, physical, and chemical properties [1,2]. HEAs are typically a solid solution containing more than five principal elements [3–5]. Configuration entropy (S) is also used as a parameter to define HEAs. It should be comparable to $\Delta S_{\text{mix}} > 1.5\ R$ for five-element alloys [6]. The high entropy plays a vital role in the stabilization of the disordered solid solution phase [7]. It forms single-phase solid solutions with a simple lattice despite having multiple components and complex chemistry. These disorder alloys have a broad spectrum of applications, such as antioxidation, anticorrosion, thermoelectric, soft magnet, and radiation tolerance materials [8–10] over conventional alloys. In 2014, another fascinating electronic property, superconductivity, was observed in a $Ta_{34}Nb_{33}Hf_8Zr_{14}Ti_{11}$ HEA with a transition temperature of 7.3 K [7]. It extends the possible applications of HEAs beyond their structural and mechanical properties-related applications. Since then, a few other HEA or medium entropy alloy superconductors have been reported, which crystallized in bcc, fcc, CsCl, hexagonal, and tetragonal crystal structures [11–15]. To date, the maximum superconducting transition temperature T_c was achieved in a $(ScZrNbTa)_{0.65}(RhPd)_{0.35}$ HEA with a CsCl lattice-type crystal structure [16]. Most of the effort on superconducting HEAs is focused on discovering new superconducting HEAs families and enhancing superconducting transition temperature using the different combinations of $3d$, $4d$, and $5d$ elements. Its multicomponent nature offers the tunability of superconducting parameters and crystal structures. Some of these alloys show exotic superconducting properties such as retention of superconducting properties in very high-pressure [17], Debye temperature in elemental range [12,15,18], and phonon-mediated superconductivity similar to binary and ternary superconducting alloys despite its highly disordered nature, where the occurrence of a regular phonon mode is unlikely. Understanding superconductivity in HEAs remains a challenge, and the unavailability of microscopic measurements on superconducting HEA makes it difficult to understand the superconducting pairing mechanism of these disordered alloys [18,19]. In this paper, we report the synthesis and detailed investigation of superconducting HEA $Nb_{0.6}Re_{0.1}Zr_{0.1}Hf_{0.1}Ti_{0.1}$ using bulk measurements of magnetization, heat capacity, and resistivity along with a microscopic probe of the vortex lattice and superconducting ground state with muon spin spectroscopy. These measurements confirmed bulk type-II superconductivity in $Nb_{0.6}Re_{0.1}Zr_{0.1}Hf_{0.1}Ti_{0.1}$ having superconducting transition temperature $T_C \simeq 5.7$ K. A superconducting ground state can be described as a nodeless isotropic gap with a moderate coupling strength and preserved time-reversal symmetry.

II. EXPERIMENTAL DETAILS

The polycrystalline sample of $Nb_{0.60}Re_{0.10}Zr_{0.10}Hf_{0.10}Ti_{0.10}$ prepared by arc melting a stoichiometric ratio of high purity elements Re (99.99%), Nb (99.99%), Hf (99.99%), Zr (99.99%), and Ti (99.99%) on water-cooled copper hearth. Titanium getter was used to absorb the oxygen, if any, present in the chamber. The sample buttons melted and flipped several times to ensure phase homogeneity. The observed weight loss was negligible during the melting. Sample composition was confirmed by energy-dispersive x-ray spectrometer, and phase purity was confirmed by x-ray diffractometer by using an X'pert PANalytical diffractometer where Cu-K_α ($\lambda = 1.5405$ Å) radiation was used. Bulk superconductivity was confirmed by magnetization measurement using a superconducting

*rpsingh@iiserb.ac.in

 ©2022 American Physical Society

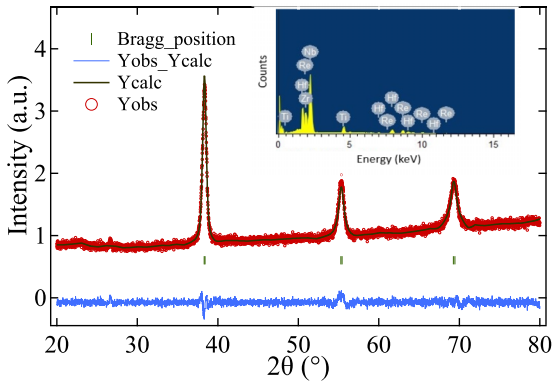

FIG. 1. Powder x-ray diffraction pattern collected at room temperature by using CuK_α radiation and energy-dispersive x-ray spectra shown in inset.

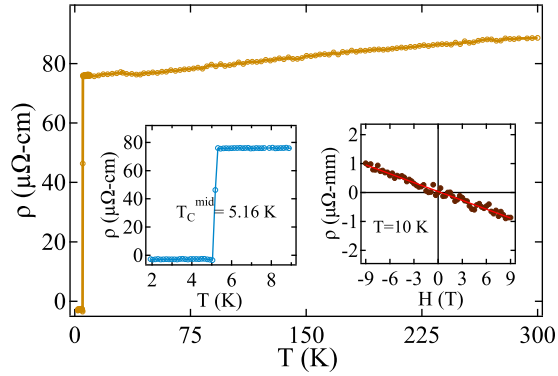

FIG. 2. The temperature-dependent resistivity in the range of 1.9 K–300 K and the left inset shows the sharp transition at 5.2(1) K. The right inset shows field-dependent resistivity at 10 K in the range ± 9 T and slope of resistivity versus magnetic field is negative.

quantum interference device from Quantum Design. Four probe and two tau methods were adopted to perform resistivity and specific heat, respectively, using a Quantum Design Physical Property Measurement System. To investigate microscopic superconducting properties, muon measurements were performed at MuSR spectrometer at ISIS Neutron and Muon Source, STFC Rutherford Appleton Laboratory, United Kingdom.

III. RESULTS AND DISCUSSION

A. Structural characterization

The x-ray data from the sample, at ambient conditions, was collected using the PANalytical X'Pert Pro instrument. The observed diffracted pattern was indexed with FULL PROF software, and the refined pattern is displayed in Fig. 1. It crystallized in centrosymmetric a bcc, space group *Im-3m*, structure with unit cell parameter $a = b = c = 3.320184(7)$ Å. The broadness of the peaks may be due to the disorder created by different radii of elements within the sample [7]. The energy-dispersive x-ray spectra was performed at five different positions (one spectra was shown in the inset of Fig. 1) on the HEA sample, which confirms the homogeneity and the averaged composition is found to be $Nb_{60}Re_{10}Zr_{10}Hf_{10}Ti_{10}$.

B. Electrical resistivity

The electrical transport study of $Nb_{0.60}Re_{0.10}Zr_{0.10}Hf_{0.10}Ti_{0.10}$ and nature was revealed by temperature-dependent resistivity measurements between temperature range 1.9 K to 300 K without applying any external field. The inset of Fig. 2 is displayed as the sharp transition T_C^{onset} at 5.30(5) K and true zero resistive value $T_C^{base} = 5.03(5)$ K. We considered the midvalue of the normal state to zero resistive states as the transition temperature $T_C^{mid} = 5.16(5)$ K. Above the transition temperature, the normal state resistivity was found to be almost temperature independent and is shown in Fig. 2. The residual resistivity ratio (ρ_{300}/ρ_{10}) is found to be 1.2, which is comparable to other HEA superconductors [12,18,20]. We have also measured Hall resistivity to study the nature of charge carrier and density in a normal state of the sample. The field-dependent Hall resistivity measurement was done at 10 K, which is shown in the inset of Fig. 2. The observed ρ (H) data was linear fit within ± 9 T magnetic field, and the slope provides the Hall coefficient $R_H = -1.08(2)\times10^{-10}$ Ω m T^{-1}. The negative sign of R_H indicates that the electrons are the charge carriers. Using the expression $R_H = -1/ne$, where n and e are the carrier density and electronic charge, respectively, this expression yields the charge carrier density $n = 6.1(1)\times10^{28}$ m^{-3}, which is comparable to the noncentrosymmetric $(HfNb)_{0.10}(MoReRu)_{0.90}$ and $(ZrNb)_{0.10}(MoReRu)_{0.90}$ HEA superconductors [18].

C. Magnetization

We have performed temperature-dependent dc magnetization in zero-field cooled warming (ZFCW) and field-cooled cooling (fcc) modes under 1 mT external magnetic field. A clear indication of a diamagnetic signal was observed, corresponding to the onset of superconducting transition temperature at $T_C = 5.60(4)$ K and is shown in Fig. 3(a). The fcc data indicates the strong pinning nature in $Nb_{0.60}Re_{0.10}Zr_{0.10}Hf_{0.10}Ti_{0.10}$ alloy. Lower critical field H_{C1} was determined using field-dependent magnetization data within a range of temperature from 1.8 K up to T_C as shown in the inset of Fig. 3(b). Up to a certain value of field, magnetization varies linearly and the point from which it starts deviating from the linearity or the Meissner line is taken as the critical field for a particular temperature. The lower critical field value H_{C1} at 0 K was estimated after fitting the data points using the Ginzburg-Landau expression:

$$H_{C1}(T) = H_{C1}(0)\left(1 - \left(\frac{T}{T_C}\right)^2\right). \quad (1)$$

The extrapolation of $H_{C1}(T)$ to 0 K yields $H_{C1}(0) = 7.95(7)$ mT.

Temperature-dependent magnetization was carried out with varying magnetic fields to estimate the upper critical field. The onset of the superconducting transition was considered as the criteria for the upper critical field, and transition temperature decreased with an increase of an applied external

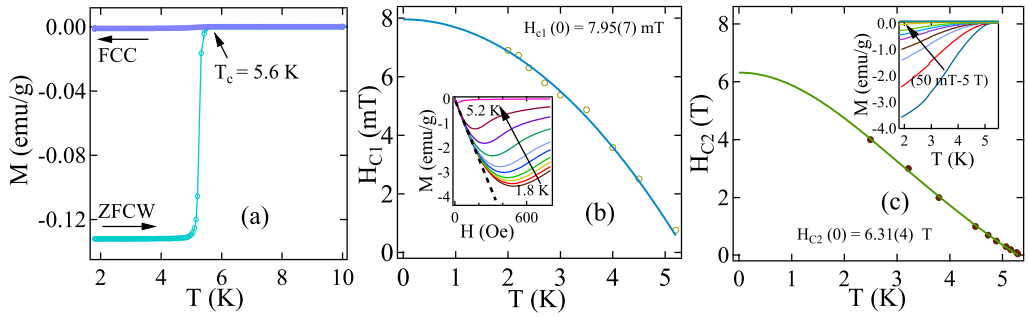

FIG. 3. (a) Temperature dependence of the dc magnetic moment in both ZFCW and fcc mode under the applied field of 1 mT (left). (b) Temperature dependence of lower critical field curved fitted with Ginzburg-Landau equation [Eq. (1)] and inset of (b) shows the field-dependent magnetization within temperature range from 1.8 K to 5.2 K (middle). (c) Temperature-dependence data of the upper critical field fitted with the Ginzburg equation [Eq. (2)] and the inset of (c) magnetization versus temperature within range of field 50 mT to 5 T is shown (right).

magnetic field, as shown in Fig. 3(c). H_{C2} versus temperature shows a linear behavior near T_C and can be described with the Ginzburg-Landau equation,

$$H_{C2}(T) = H_{C2}(0)\left(\frac{(1-t^2)}{(1+t^2)}\right), \tag{2}$$

where $t = T/T_C$ is the reduced temperature; the fitting reveals the upper critical value at 0 K is 6.31(4) T. The Ginzburg-Landau coherence length parameter can be evaluated using the value of $H_{C2}(0)$ according to the expression

$$H_{C2}(0) = \frac{\Phi_0}{2\pi\xi_{\rm GL}^2}, \tag{3}$$

where Φ_0 is the flux quantum ($\Phi_0 = 2.07\times10^{-15}$T m^2) and substituting the $H_{C2}(0) = 6.31(4)\,T$, we get coherence length $\xi_{\rm GL}(0) = 7.2(1)$ nm. The magnetic penetration depth $\lambda_{\rm GL}(0)$ depends on the lower critical field $H_{C1}(0)$ and $\xi_{\rm GL}(0)$ according to the expression

$$H_{C1}(0) = \frac{\Phi_0}{4\pi\lambda_{\rm GL}^2(0)}\left(\ln\frac{\lambda_{\rm GL}(0)}{\xi_{\rm GL}(0)} + 0.12\right). \tag{4}$$

After substituting the calculated parameters $H_{C1}(0) = 7.95(7)$ mT and $\xi_{\rm GL}(0) = 7.2(1)$ nm, we obtained $\lambda_{\rm GL}(0) = 279(2)$ nm. The Ginzburg-Landau parameter $\kappa_{\rm GL}$ differentiates the type of superconductivity and is expressed as $\kappa_{\rm GL} = \frac{\lambda_{\rm GL}(0)}{\xi_{\rm GL}(0)}$. For $\xi_{\rm GL} = 7.2(1)$ nm and $\lambda_{\rm GL}(0) = 279(2)$ nm, we obtained $\kappa_{\rm GL} = 39(1) \gg \frac{1}{\sqrt{2}}$, indicating that the $Nb_{60}Re_{10}Zr_{10}Hf_{10}Ti_{10}$ HEA is a strong type-II superconductor. In type-II superconductors, the applied magnetic field is responsible for breaking the Cooper pair by two types of mechanisms: orbital and Pauli limiting effects [21]. For BCS superconductors, the orbital limiting field $H_{C2}^{\rm orb}(0)$ is calculated via the Werthamar-Helfand-Hohenberg model,

$$H_{C2}^{\rm orbital}(0) = -\alpha T_C \left.\frac{dH_{C2}(T)}{dT}\right|_{T=T_C}, \tag{5}$$

where α can take 0.693 value in the dirty limit. The ratio of BCS coherence length and electronic mean free path value $\xi_0/l > 1$ (detailed in Sec. III F) and suggest the dirty limit superconductivity in $Nb_{0.60}Re_{0.10}Zr_{0.10}Hf_{0.10}Ti_{0.10}$. The slope of the temperature-dependent upper critical field $\frac{dH_{C2}}{dT}$ at T = T_C is estimated to be $-1.08(3)$ T, which yields $H_{C2}^{\rm orb} = 4.2(1)$ T, and another effect, Pauli limiting field H_P can be addressed within the BCS theory using the expression $H_{c2}^{P} = 1.84\ T_C$ and the estimate value of $H_{C2}^{P} = 10.3(1)$ T.

To measure the relative strength of the orbital and Pauli limiting field, the Maki parameter is calculated and expressed as $\alpha_M = \sqrt{2}H_{C2}^{\rm orb}(0)/H_{C2}^{p}(0)$. The value obtained for $\alpha_M = 0.57$, suggesting the small influence of the paramagnetic effect and mainly the orbital limiting field is responsible for pair breaking.

D. Specific heat

The specific-heat measurement was performed on a $Nb_{0.60}Re_{0.10}Zr_{0.10}Hf_{0.10}Ti_{0.10}$ alloy, applying external field and in zero field. The sample was mounted on the platform with Apiezon N grease to establish good thermal contact. A pronounced jump in heat capacity was observed at transition temperature T_C at 5.4(1) K as shown in Fig. 4(a). The T_C value estimated by-specific heat measurement is comparable with resistivity and magnetization. The specific-heat data in the normal state (above T_C) was well fitted with the following equation:

$$\frac{C}{T} = \gamma_n + \beta_3 T^2. \tag{6}$$

This fitting provides the electronic parameter (Sommerfeld coefficient) $\gamma_n = 7.1(1)$ mJmol^{-1}K^{-2} and the lattice contribution parameter to the specific heat, $\beta_3 = 0.140(2)$ mJmol^{-1}K^{-4}. Both parameters γ_n and β_3 have paramount importance in calculating the density of states [$D_c(E_F)$], Debye temperature (θ_D), and electron-phonon coupling constant (λ_{e-p}). The following quantities are calculated from the expressions provided in Ref. [21] and the estimated values are $D_c(E_F) = 3.01(4)$ $\frac{\rm states}{eV\,f.u}$, $\theta_D = 240(1)$ K, and $\lambda_{e-p} = 0.70$. The value of electron phonon coupling strength λ_{e-p} is comparable with other HEA superconductors [11,22], which suggests moderately coupled superconductivity in $Nb_{0.60}Re_{0.10}Zr_{0.10}Hf_{0.10}Ti_{0.10}$.

To further reveal the superconducting ground-state behavior, electronic specific heat $C_{\rm el}$ in the superconducting state can be estimated by excluding the phonon contribution from the total specific heat $C(T)$ by the expression

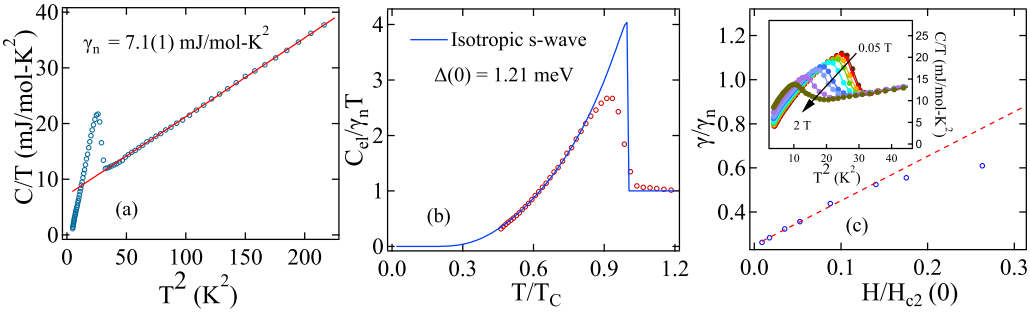

FIG. 4. (a) C/T versus T^2 curve above T_C fitted by Eq. (8). (b) The observed data shown by red square circle was fitted with BCS isotropic gap (blue line) equation. (c) Normalized γ of superconducting state is plotted with normalized field. Dashed red curve represents the linear behavior at lower values and indicates the *s*-wave superconductivity.

$C_{\rm el} = C(T) - \beta_3 T^3$. For a single gap BCS superconductor, the normalized entropy in the superconducting state is given by

$$\frac{S}{\gamma_n T_C} = -\frac{6}{\pi^2}\left(\frac{\Delta(0)}{k_B T_C}\right)\int_0^\infty [f\ln(f) + (1-f)\ln(1-f)]dy, \tag{7}$$

where $f(\xi) = [\exp(E(\xi)/k_B T) + 1]^{-1}$ is the Fermi function, $E(\xi) = \sqrt{\xi^2 + \Delta^2(t)}$, where $E(\xi)$ is the energy of the normal electrons relative to the Fermi energy, $y = \xi/\Delta(0), t = T/T_C$, and $\Delta(t) = \tanh[1.82\{1.018[(1/t) - 1]\}^{0.51}]$ is the BCS approximation for the energy gap. The normalized electronic specific heat below T_C is related to the first derivative of normalized entropy as

$$\frac{C_{\rm el}}{\gamma_n T_C} = t\frac{d(S/\gamma_n T_C)}{dt}. \tag{8}$$

The fitting provides the superconducting gap value $\frac{\Delta(0)}{k_B T_C} = 2.57$, which is very high in magnitude with respect to the BCS predicted value and slightly more than the equimolar $Nb_{20}Re_{20}Zr_{20}Hf_{20}Ti_{20}$ HEA [23]. The electronic heat capacity data together with electron phonon coupling strength provide the evidence of isotropic *s* wave moderately coupled superconductivity in $Nb_{60}Re_{10}Zr_{10}Hf_{10}Ti_{10}$. We carried out field-dependent specific-heat measurements to further unveil the superconducting gap structure. We first calculated the electronic specific heat with respective fields by subtracting the corresponding phononic part ($\beta_3 T^3$) from total specific heat (C). The field-dependent electronic specific heat in the superconducting state was fitted with the expression [24]

$$\frac{C_{\rm el}}{T} = \gamma + \frac{A}{T}\exp\left(\frac{-bT_c}{T}\right). \tag{9}$$

Here A is a material-dependent quantity and $b = \frac{\Delta(0)}{k_B T_c}$ superconducting gap. Figure 4(c) shows the normalized γ rises linearly with applied external magnetic field H, and both parameters γ and H are normalized by γ_n and the upper critical field $H_{C2}(0)$, respectively. The linear increase in γ is because the quasiparticle excitation is confined within the vortex cores, and a number of vortices vary with field H for an isotropic superconducting gap structure [24,25]. Thus, the linear behavior of $\gamma(H)$ proportional to field H at low fields indicates the fully isotropic *s*-wave superconducting gap. In the presence of nodes, the $\gamma(H)$ is expected to vary as a square root to the applied field.

E. μSR spectroscopy

Muon spin relaxation in zero fields and muon spin rotation in transverse field measurements were done on a MuSR spectrometer ISIS facility at Rutherford Appleton Laboratory, United Kingdom. Forty pulses of spin-polarized muons enter MuSR in each second, which are implanted into the sample, and these muons sits at the interstitial positions in the powder sample. The muon spin precess with Larmor frequency decays into a positron and two neutrinos. The positron decay into the initial muon spin direction is recorded through 64 scintillator detectors, and these detectors are positioned in a circular design around the sample chamber. Two sets of detectors were positioned around the sample in zero field muon spin relaxation measurements. In contrast, in transverse field muon spin rotation, the detectors were positioned in four configurations, and each configuration consisted of 16 detectors named forward, backward, top, and bottom. The time-domain asymmetry spectra were calculated using the expression A(t) $= (\frac{F(t)-\alpha B(t)}{F(t)+\alpha B(t)})$, and α is the relative efficiency of counts between any two of the four detectors [26]. This asymmetry function gives information regarding muon spin polarization at a timescale. The powder sample was mixed with GE varnish and mounted on a silver holder. The benefits of using a silver holder are getting a time-independent signal in ZF-μSR and a nondecaying oscillation in TF-μSR configurations. The low temperature was achieved using ^{3}He sorption cryostat. In the ZF configuration, the sample was first cooled to the lowest temperature in the zero field, and then data was taken while warming without any applied field. The effect of the magnetic field at sample position due to the earth's magnetic field or from the neighboring instruments are canceled by a set of correction coil. In TF configuration, an external magnetic field was applied perpendicular to the direction of muon spin. The sample was field cooled to create a flux line lattice, and data were taken from base temperature to above the transition temperature.

1. ZF-μSR relaxation

μSR measurements in zero field can be used to detect spontaneous magnetization associated with broken time-reversal symmetry in the superconducting state. We collected the relaxation spectra above and far below the superconducting transition temperature, which is shown in Fig. 5(a). The decaying relaxation behavior indicates that no oscillation is

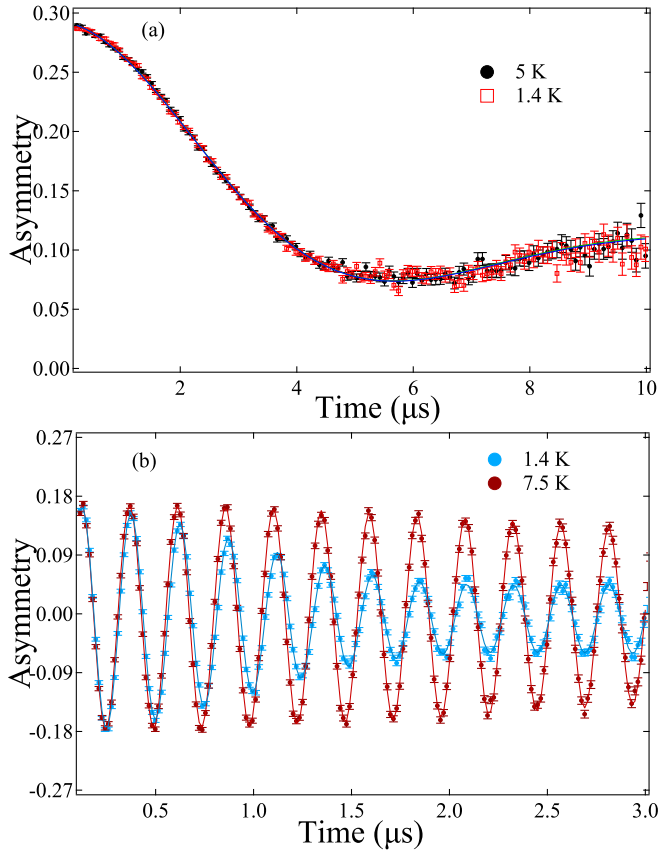

FIG. 5. (a) Zero-field μSR asymmetry spectra is shown from above and below T_C. The black line represents the fit to the Kubo-Toyabe equation. (b) Transverse field μSR asymmetry spectra collected at 1.39 K and 7.5 K under an applied field of 30 mT. These red and blue lines are the fit to the data using Eq. (12).

present above and below T_C, and the relaxation comes from the randomly oriented nuclear moments. ZF-μSR relaxation data above and below T_C were fitted very well with the Kubo-Toyabe equation, which is given as [27]

$$G_{\mathrm{KT}}(t) = \frac{1}{3} + \frac{2}{3}(1 - \sigma_{\mathrm{ZF}}^2 t^2)\exp\left(\frac{-\sigma_{\mathrm{ZF}}^2 t^2}{2}\right), \qquad (10)$$

where σ_{ZF} is the muon spin relaxation rate. The asymmetry spectra can be explained with expression as

$$A(t) = A_1 G_{\mathrm{KT}}(t)\exp(-\Lambda t) + A_{\mathrm{BG}}. \qquad (11)$$

Here A_1 is the sample asymmetry, A_{BG} is the background asymmetry signal coming due to the stopping of muons in the sample holder, and Λ is electronic relaxation rate. The fitting of Eq. (11) above and below the T_C yield no noticeable change of relaxation rate in the detection limit (10 μT) of instruments. The change corresponding to both relaxations are found as $\sqrt{\Delta}/\gamma_\mu = 0.01$ Oe and $\Lambda/\gamma_\mu = 0.04$ Oe, which are outside the detection limit for the MuSR instrument. Hence, the time-reversal symmetry is preserved in $Nb_{60}Re_{10}Zr_{10}Hf_{10}Ti_{10}$.

2. TF-μSR

TF-μSR measurements have been performed on $Nb_{0.60}Re_{0.10}Zr_{0.10}Hf_{0.10}Ti_{0.10}$ alloys to get insight into superconducting gap symmetry and the field distribution in the mixed state. We first cool the sample in an applied magnetic field of 30 mT, which is greater than the lower critical field but less than the H_{c2} ($H_{c1} < H^{\mathrm{ext}} \ll H_{C2}$) to create a well-ordered flux line lattice. Asymmetry spectra in TF-μSR were recorded in the temperature range from 1.39 K to 7.5 K and only two spectra at 1.39 K, and above T_C are displayed in Fig. 5(b). The distribution of field in the entire temperature scale was extracted from the TF-μSR time spectra by the maximum entropy method [28]. Below the T_C, Fig. 6(c) shows evidence of depolarization and the inset of Fig. 6(c) clearly shows the homogeneous field above T_C. The variation of the muon precession in asymmetry spectra was observed because of the interaction of muon spin with internal field distribution in a sample. Above T_C, muon spin relaxes due to the presence of randomly oriented nuclear dipolar moments, and below T_C, the relaxation arises from the inhomogeneous magnetic field due to the formation of flux line lattice in the mixed state plus the nuclear contribution. The asymmetry spectra of TF-μSR is well fitted in all temperature ranges by the Gaussian oscillatory decaying function and is described below as [29,30]

$$A(t) = \sum_{i=1}^{N} A_i \exp\left(-\frac{1}{2}\sigma_i^2 t^2\right)\cos(\gamma_\mu B_i t + \phi) + A_{bg}\cos(\gamma_\mu B_{bg} t + \phi), \qquad (12)$$

where A_i and A_{bg} are the sample and sample holder related asymmetry signal, respectively, ϕ is the initial phase offset, and σ is rate of Gaussian depolarization of muon spin. B_i is the mean-field contribution of the ith component of the Gaussian distribution, and B_{bg} is the background field contribution coming from the sample holder.

Above T_C, there is a constant relaxation rate that occurs due to the random orientation of the magnetic moment of nuclear spins and is temperature independent. The internal field dependence on temperature is shown in Fig. 6(b), which shows a background magnetic field contribution that is constant for the temperature range measured. The internal magnetic field distribution in the mixed state denoted by $\langle B \rangle$ is less than the applied fields for $T < T_C$, which clearly shows the Meissner field expulsion in the superconducting state. At temperature ($T > T_C$), it again recovers the applied field value and overlaps with the background signal. The total depolarization rate is not only from the flux lattice (σ_{FLL}) but also arises due to the nuclear magnetic moment (σ_n), which is temperature independent. The σ_n contribution was calculated from the above T_C data points and σ_{FLL} is estimated from subtracting the contribution of σ_n from the total depolarization rate as $\sigma_{\mathrm{FLL}}^2 = \sigma^2 - \sigma_n^2$, where σ is the total depolarization rate. σ_{FLL} is related to the London penetration depth via ($\sigma_{\mathrm{FLL}} \propto 1/\lambda^{-2}$). For small applied fields where H << H_{C2}, the inverse square of the London penetration depth can be calculated via the formula

$$\frac{\sigma_{\mathrm{FLL}}^2(T)}{\gamma_\mu^2} = \frac{0.00371\Phi_0^2}{\lambda^4(T)}, \qquad (13)$$

where Φ_0 is the magnetic flux quantum and $\gamma_\mu/2\pi = 135.5$ MHz/T is muon gyromagnetic ratio. Within London

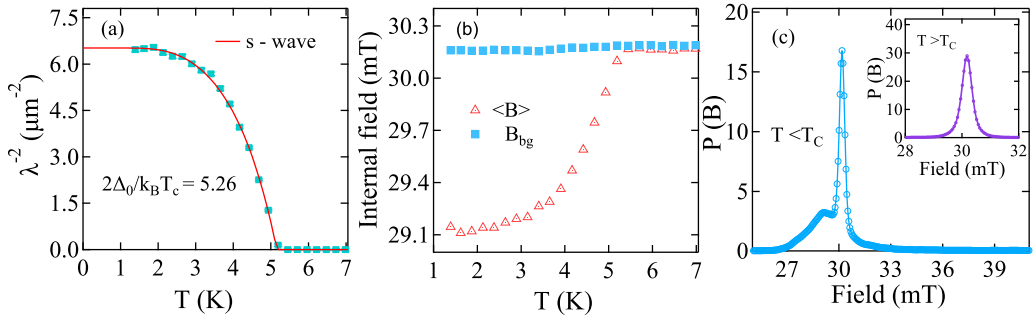

FIG. 6. (a) Temperature-dependent variation of λ^{-2} fitted well with isotropic *s*-wave BCS superconducting model. (b) Internal magnetic field distribution inside the sample with respect to temperature. Red data points are the observed field from the sample, and blue data points are the background field contribution from the sample holder. (c) Field distribution in vortex state and normal state [inset of Fig. 6(c)].

approximation, the calculated London penetration depth at 0 K is $\lambda^{\mu} = 391(18)$ nm, which is a bit higher than the calculated value of $\lambda = 279(2)$ nm from magnetization. The temperature dependence of the penetration depth for *s*-wave BCS superconducting gap is given by the expression [31–33]

$$\frac{\lambda^{-2}(T)}{\lambda^{-2}(0)} = 1 + 2\int_{\Delta(T)}^{\infty}\left(\frac{\partial f}{\partial E}\right)\frac{EdE}{\sqrt{E^2-\Delta(T)^2}}, \tag{14}$$

where $\lambda(0)$ is the London penetration depth at 0 K, and $f = [1+\exp(E/k_BT)]^{-1}$ is the Fermi function and Δ (T) is the BCS superconducting gap function which is defined by Δ (T) = $\Delta_0\tanh[1.82\{1.018[(T_C/T)-1]\}^{0.51}]$. The experimental data of λ^{-2} (T) was best fitted with the BCS s-wave modal given by Eq. (14) and the obtained $T_C = 5.2(2)$ K is also in good agreement with the values measured from magnetization and specific-heat measurements for $Nb_{60}Re_{10}Zr_{10}Hf_{10}Ti_{10}$. The ratio of the superconducting gap at 0 K, $\Delta_0/k_BT_c = 2.65(5)$, which shows great deviation from the BCS value (1.73), and is comparable to the estimated value by specific heat measurement [2.57(8)].

F. Electronic property

To supplement the observed result of the experiment measurements, we have determined the electronic parameter such as the BCS coherence length, electronic mean free path, and the Fermi velocity. We have used the estimated parameter charge carrier density (measured from Hall measurement) shown in the inset of Fig. 2, Sommerfeld coefficient by normal heat capacity, and resistivity at transition temperature. The Sommerfeld coefficient is related with effective mass and carrier density of the quasiparticle by the equation [34]

$$\gamma_n = \left(\frac{\pi}{3}\right)^{2/3}\frac{k_B^2 m^* n^{1/3}}{\hbar^2}, \tag{15}$$

where k_B, n, and m^* are the Boltzmann constant, carrier density, and effective mass of the quasiparticle, respectively. Using the values of Sommerfeld coefficient $\gamma_n = 7.1(1)$ mJ $-$ mol^{-1}K^{-2} and carrier density $n = 6.1(1)\times10^{28}$m^{-3}, we estimated the effective mass of quasiparticle $m^* = 9.9(2)\,m_e$.

The Fermi velocity is directly related to the carrier density and effective mass, which can be expressed as

$$n = \frac{1}{3\pi^2}\left(\frac{m^* v_f}{\hbar}\right)^3. \tag{16}$$

Using the estimated value of effective mass $m^* = 9.9\,m_e$ and carrier density $n = 6.1(1)\times10^{28}$m^{-3} of quasiparticle, we get the Fermi velocity $v_F = 1.5\times10^5$ ms^{-1}.

The mean-free path is dependent on Fermi velocity v_f, effective mass m^*, and the residual resistivity by the expression

$$l = \frac{3\pi^2\hbar^3}{e^2\rho_0 m^{*2} v_F^2}. \tag{17}$$

The previous estimated value of Fermi velocity and effective mass with the residual resistivity $\rho_0 = 76(1)\,\mu\Omega-$cm, which yield mean-free path $l = 9.6$ Å. BCS coherence length can be estimated using Fermi velocity and transition temperature by the expression as

$$\xi_0 = \frac{0.18\hbar v_F}{k_B T_C}. \tag{18}$$

Using the Fermi velocity parameter value and transition temperature $T_C = 5.6$ K, we get the ratio of BCS coherence

TABLE I. Superconducting and normal state parameters of $Nb_{60}Re_{10}Zr_{10}Hf_{10}Ti_{10}$.

Parameters	Unit	$Nb_{0.6}Re_{0.1}Zr_{0.1}Hf_{0.1}Ti_{0.1}$
T_C^{dc}	K	5.60(4)
$H_{C1}(0)$	mT	7.95(7)
$H_{C2}(0)$	T	6.31(1)
$H_{C2}^{P}(0)$	T	10.3(1)
$\xi_{GL}^{H_{c1}}$	nm	7.2(1)
$\lambda_{GL}^{H_{c1}}$	nm	279(2)
$\lambda(0)^{\mu SR}$	nm	391(18)
$k_{GL}^{H_{c1}}$		39(1)
$\Delta(0)/k_BT_C$ (specific heat)		2.57(8)
$\Delta(0)/k_BT_C(\mu SR)$		2.65(5)
m^*/m_e^{Hall}		9.9(2)
$m^*/m_e^{(\gamma_n,\lambda^{\mu})}$		9.3(3)
ξ_0/l_e		38(5)
v_F^{Hall}	10^5 ms^{-1}	1.50(4)
n^{Hall}	10^{28} m^{-3}	6.1(1)
$n^{(\gamma_n,\lambda^{\mu})}$	10^{28} m^{-3}	7.1(5)
T_F^{Hc1}	K	6480(236)
$T_F^{\mu SR}$	K	7590(600)

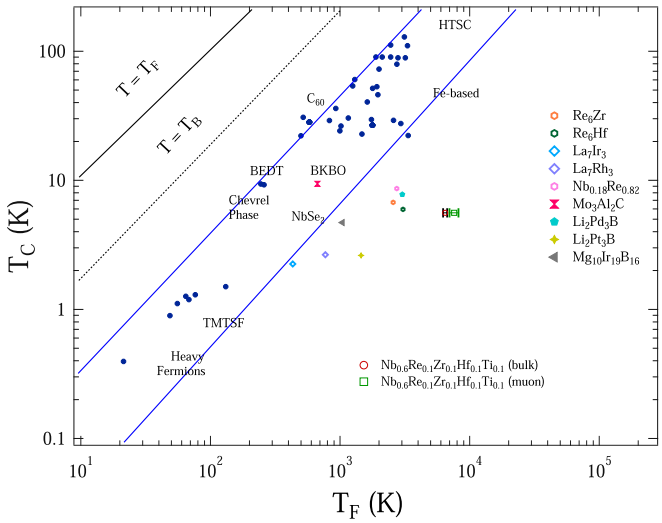

FIG. 7. Uemura plot representing the superconducting transition temperature versus Fermi temperature for different superconducting families. Two solid blue lines represent the unconventional band of superconductors and the solid red circle for $Nb_{60}Re_{10}Zr_{10}Hf_{10}Ti_{10}$ alloy away from the unconventional band.

length to electronic mean-free path $\xi(0)/l = 38 > 1$, which strongly suggests that the sample is in the dirty limit of superconductivity. Other estimated parameters are listed in Table I.

The Fermi temperature can be expressed as $k_B T_F = \frac{\hbar^2}{2m^*}(3\pi^2 n)^{2/3}$, where k_B, $m^* = 9.9(2)\ m_e$, and $n = 6.1(1)\times 10^{28}\mathrm{m}^{-3}$ are the Boltzmann constant, effective mass, and carrier density of the quasiparticle, respectively. The expression gives Fermi temperature, T_F 6480(236) K, while using the penetration depth by H_{C1}. We have also calculated the Fermi temperature $T_F = 7590(600)\,\mathrm{K}$ by measuring penetration depth via μSR, and more details of the calculations can be found in Refs. [35,36].

Uemura *et al.* [37–39] give a classification to distinguish the conventional and unconventional nature of superconductor by the ratio of T_C/T_F. The range of unconventional superconductor is $0.01 \leqslant T_C/T_F \leqslant 0.1$, and the rest of the range represents the conventional superconductor. The ratios of T_C/T_F are 0.00086 (via H_{C1}) and 0.00073 (via muSR) (see Fig. 7), places $Nb_{60}Re_{10}Zr_{10}Hf_{10}Ti_{10}$ away from the unconventional superconductor line, and categories it as a conventional superconductor.

IV. CONCLUSION

A detailed investigation of the superconducting and normal state properties of the superconducting HEA $Nb_{60}Re_{10}Zr_{10}Hf_{10}Ti_{10}$ has been conducted, using detailed magnetization, electrical resistivity, heat capacity, and μSR measurements. It is a type-II superconductor with a nodeless, isotropic superconducting gap and is well described by the BCS theory in the dirty limit. In the superconducting ground state, time-reversal symmetry has been preserved in the detection limit of μSR experiments. The calculated electronic properties of the superconducting state suggest the similarity with binary and ternary superconducting compounds. Uemura plot placed it in the same region as a conventional superconductor. To understand the HEA superconducting ground state and pairing mechanism in detail, it is essential to search and perform a microscopic study of new superconducting HEAs.

ACKNOWLEDGMENTS

K.M. acknowledges the Council of Scientific and Industrial Research (CSIR), Government of India, for providing a SRF Fellowship (Award No. 09/1020(0123)/2017-EMR-I). R.P.S. acknowledges the Science and Engineering Research Board, Government of India for the Core Research Grant No. CRG/2019/001028. We thank ISIS, STFC, UK for the beamtime to perform the μSR experiments.

[1] W. Dong, Z. Zhou, M. Zhang, Y. Ma, P. Yu, P. K. Liaw, and G. Li, Metals **9**, 867 (2019).
[2] F. V. Rohr, M. J. Winiarski, J. Tao, T. Klimczuk, and R. J. Cava, Proc. Natl. Acad. Sci. USA **113**, E7144 (2016).
[3] E. J. Pickering and N. G. Jones, Int. Mater. Rev. **61**, 183 (2016).
[4] Y. Xu, C. Li, Z. Huang, Y. Chen, and L. Zhu, Entropy **22**, 786 (2020).
[5] M. C. Gao, P. Gao, F. Zhang, L. Z. Ouyang, M. Widom, and J. A. Hawk, Curr. Opin. Solid State Mater. Sci. **21**, 238 (2017).
[6] X. Wang, W. Guo, and Y. Fu, J. Mater. Chem. A **9**, 663 (2021).
[7] P. Koželj, S. Vrtnik, A. Jelen, S. Jazbec, Z. Jagličić, S. Maiti, M. Feuerbacher, W. Steurer, and J. Dolinšek, Phys. Rev. Lett. **113**, 107001 (2014).
[8] M.-H. Tsai and J.-W. Yeh, Mater. Res. Lett. **2**, 107 (2014).
[9] Y. Zhang, T. T. Zuo, Y. Q. Cheng, and P. K. Liaw, Sci. Rep. **3**, 1455 (2013).
[10] Y. Lin, T. Yang, L. Lang, C. Shan, H. Deng, W. Hu, and F. Gao, Acta Mater. **196**, 133 (2020).
[11] B. Liu, J. Wu, Y. Cui, Q. Zhu, G. Xiao, H. Wang, S. Wu, G. Cao, and Z. Ren, ACS Appl. Electron. Mater. **2**, 1130 (2020).
[12] K. Stolze, F. A. Cevallos, T. Kong, and R. J. Cava, J. Mater. Chem. C **6**, 10441 (2018).
[13] N. Ishizu and J. Kitagawa, arXiv:2007.00788.
[14] B. Liu, J. Wu, Y. Cui, Q. Zhu, G. Xiao, S. Wu, G. Cao, and Z. Ren, Scr. Mater. **182**, 109 (2020).
[15] S. Marik, K. Motla, M. Varghese, K. P. Sajilesh, D. Singh, Y. Breard, P. Boullay, and R. P. Singh, Phys. Rev. Mater. **3**, 060602(R) (2019).
[16] K. Stolze, J. Tao, F. V. Rohr, T. Kong, and R. J. Cava, Chem. Mater. **30**, 906 (2018).
[17] J. Guo, H. Wang, F. V. Rohr, Z. Wang, S. Cai, Y. Zhou, K. Yang, A. Li, S. Jiang, Q. Wu, R. J. Cava, and L. Sun, Proc. Natl. Acad. Sci. USA **114**, 13144 (2017).
[18] K. Motla, Arushi, P. K. Meena, D. Singh, P. K. Biswas, A. D. Hillier, and R. P. Singh, Phys. Rev. B **104**, 094515 (2021).
[19] L. Sun and R. J. Cava, Phys. Rev. Mater. **3**, 090301 (2019).

[20] S. Vrtnik, P. Kozelj, A. Meden, S. Maiti, W. Steurer, M. Feuerbacher, and J. Dolinsek, J. Alloys Compd. **695**, 3530 (2017).
[21] D. Singh, A. D. Hillier, A. Thamizhavel, and R. P. Singh, Phys. Rev. B **94**, 054515 (2016).
[22] J. Wu, B. Liu, Y. Cui, Q. Zhu, G. Xiao, H. Wang, S. Wu, G. Cao, and Z. Ren, Sci. China Mater. **63**, 823 (2020).
[23] S. Marik, M. Varghese, K. P. Sajilesh, D. Singh, and R. P. Singh, J. Alloys Compd. **769**, 1059 (2018).
[24] M. Isobe, M. Arai, and N. Shirakawa, Phys. Rev. B **93**, 054519 (2016).
[25] N. Nakai, P. Miranovic, M. Ichioka, and K. Machida, Phys. Rev. B **70**, 100503(R) (2004).
[26] A. D. Hillier, J. S. Lord, K. Ishida, and C. Rogers, Philos. Trans. R. Soc. A **377**, 20180064 (2019).
[27] R. S. Hayano, Y. J. Uemura, J. Imazato, N. Nishida, T. Yamazaki, and R. Kubo, Phys. Rev. B **20**, 850 (1979).
[28] B. D. Rainford and G. J. Daniell, Hyperfine Interact. **87**, 1129 (1994).
[29] M. Weber, A. Amato, F. N. Gygax, A. Schenck, H. Maletta, V. N. Duginov, V. G. Grebinnik, A. B. Lazarev, V. G. Olshevsky, V. Yu. Pomjakushin, S. N. Shilov, V. A. Zhukov, B. F. Kirillov, A. V. Pirogov, A. N. Ponomarev, V. G. Storchak, S. Kapusta, and J. Bock, Phys. Rev. B **48**, 13022 (1993).
[30] A. Maisuradze, R. Khasanov, A. Shengelaya, and H. Keller, J. Phys.: Condens. Matter **21**, 075701 (2009).
[31] B. S. Chandrasekhar and D. Einzel, Ann. Phys. **505**, 535 (1993).
[32] R. Prozorov and R. W. Giannetta, Supercond. Sci. Technol. **19**, R41 (2006).
[33] D. T. Adroja, A. Bhattacharyya, M. Telling, Y. Feng, M. Smidman, B. Pan, J. Zhao, A. D. Hillier, F. L. Pratt, and A. M. Strydom, Phys. Rev. B **92**, 134505 (2015).
[34] M. Tinkham, *Introduction to Superconductivity* (McGraw-Hill, New York, 1996).
[35] D. Singh, J. A. T. Barker, A. Thamizhavel, D. McK. Paul, and R. P. Singh, J. Phys.: Condens. Matter **30**, 075601 (2018).
[36] A. D. Hillier and R. Cywinski, Appl. Magn. Reson. **13**, 95 (1997).
[37] Y. J. Uemura, V. J. Emery, A. R. Moodenbaugh, M. Suenaga, D. C. Johnston, A. J. Jacobson, J. T. Lewandowski, J. H. Brewer, R. F. Kiefl, S. R. Kreitzman, G. M. Luke, T. Riseman, C. E. Stronach, W. J. Kossler, J. R. Kempton, X. H. Yu, D. Opie, and H. E. Schone, Phys. Rev. B **38**, 909 (1988).
[38] Y. J. Uemura, G. M. Luke, B. J. Sternlirb, J. H. Brewer, J. F. Carolan, W. N. Hardy, R. Kadono, J. R. Kempton, R. F. Kiefl, S. R. Kreitzman, P. Mulhern, T. M. Riseman, D. L. Williams, B. X. Yang, S. Uchida, H. Takagi, J. Gopalakrishnan, A. W. Sleight, M. A. Subramanian, C. L. Chien *et al.*, Phys. Rev. Lett. **62**, 2317 (1989).
[39] Y. J. Uemura, L. P. Le, G. M. Luke, B. J. Sternlieb, W. D. Wu, J. H. Brewer, T. M. Riseman, C. L. Seaman, M. B. Maple, M. Ishikawa, D. G. Hinks, J. D. Jorgensen, G. Saito, and H. Yamochi, Phys. Rev. Lett. **66**, 2665 (1991).